

SUPPLEMENTARY INFORMATION

Defect-free MoS₂-flakes/amorphous-carbon Hybrid as Advanced Anode for Lithium-ion Batteries

Duc Anh Dinh^{1*}, Tuan Loi Nguyen^{2,3}, Tran Viet Cuong¹, Kwan San Hui⁴, Trung Hieu Bui¹,
Shuxing Wu⁵, Kwun Nam Hui^{6*}

¹NTT hi-tech insitute, Nguyen Tat Thanh university, Ho Chi Minh city 700000, Vietnam

²Institute of Fundamental and Applied Sciences, Duy Tan University, Ho Chi Minh City, 700000,
Vietnam

³Faculty of Environmental and Chemical Engineering, Duy Tan University, Da Nang, 550000,
Vietnam

⁴Engineering, University of East Anglia, Norwich, NR4 7TJ, United Kingdom

⁵School of Chemical Engineering and Light Industry, Guangdong University of Technology,
Guangzhou 510006, PR China

⁶Institute of Applied Physics and Materials Engineering, University of Macau, Avenida da
Universidade, Taipa, Macau, China

*Corresponding author:

E-mail: ddanh@ntt.edu.vn (Duc Anh Dinh)

E-mail: bizhui@um.edu.mo (Kwun Nam Hui)

S1. Raman analysis of bulk and exfoliated MoS₂

Raman spectroscopy measurements, reported in Figure 1c of the main text, are carried out to investigate the vibrational modes of exfoliated MoS₂ with respect to that of bulk MoS₂. Figure S1 shows the statistical Raman analysis of the peaks position difference of the A_{1g}(Γ) and E_{2g}¹(Γ) modes, *i.e.* Pos(A_{1g}) - Pos(E_{2g}¹), full width at half maximum values of the A_{1g} and E_{2g}¹ (FWHM(E_{2g}¹) and FWHM(A_{1g})) for exfoliated MoS₂ (Fig. 1a, b and c, respectively), and bulk MoS₂ (Fig. 1d, e and f, respectively).

According to the statistical Raman analysis shown in Figure 3a and d, the peaks position difference values between the A_{1g} and E_{2g}¹ modes, *i.e.* Pos(A_{1g}) - Pos(E_{2g}¹) are ~ 26 cm⁻¹ for bulk MoS₂ and ~ 25 cm⁻¹ for exfoliated MoS₂, respectively. The decrease in peaks position difference value of exfoliated MoS₂ with respect to bulk MoS₂ indicates the decrease in the number of MoS₂ layers after the exfoliation process.¹⁻³ Also, both FWHM(A_{1g}) and FWHM(E_{2g}¹) of exfoliated MoS₂ flakes increase ~ 1 cm⁻¹ with respect to the corresponding modes of bulk MoS₂, see Figure 3b, c, e and f. The increase of FWHM(E_{2g}¹) and FWHM(A_{1g}) for exfoliated MoS₂ is attributed to the variation of interlayer force constants between the inner and outer layers.³

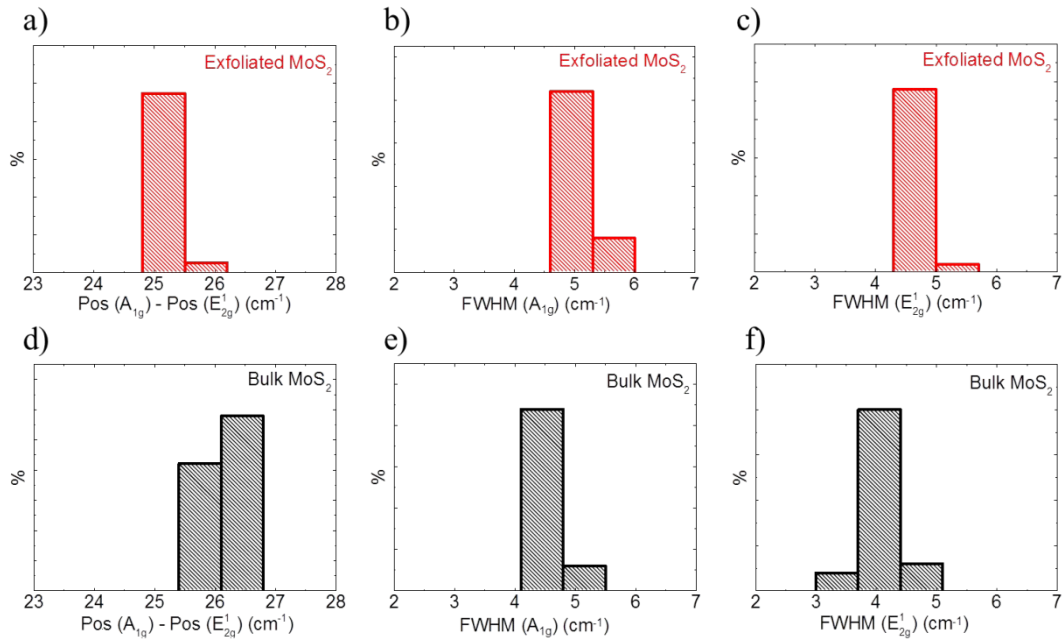


Figure S1. Statistical Raman analysis of (a), (d) Pos(A_{1g}) - Pos(E_{2g}¹); (b), (e) FWHM(E_{2g}¹) and (c), (f) FWHM(A_{1g}) for bulk and exfoliated MoS₂

S2. Optical absorption spectroscopy of exfoliated MoS₂

The exfoliated MoS₂ flakes are studied by optical absorption spectroscopy (OAS). The optical absorption spectra are acquired with a Cary Varian 5000UV-Vis spectrophotometer with 1 nm resolution. Measurements are carried out in the 250-800 nm range, limited by the strong absorption features of 2-propanol (IPA) (cut-off wavelength 240 nm). The absorption spectra were acquired using a 1 mL quartz glass cuvette. Briefly, the UV-vis spectrum of the exfoliated MoS₂ exhibits the

typical excitonic peaks at: (A) 660 nm and (B) 604 nm, ascribed to excitons associated with the direct gap transition at the K point of the Brillouin zone in 2D MoS₂⁴⁻⁶; (C) 441 nm and (D) 383 nm due to excitonic transitions from the valence band to the conduction band.⁵⁻⁷ The concentration of MoS₂ flakes in IPA can be estimated to be 0.03 g L⁻¹ from the optical absorption coefficient at 672 nm, using $A = \alpha lc$ where l (m) is the light path length, c (g L⁻¹) is the concentration of the dispersed flakes, and α (L g⁻¹ m⁻¹) is the absorption coefficient, with $\alpha \approx 3400$ L g⁻¹ m⁻¹ at 672 nm.⁸

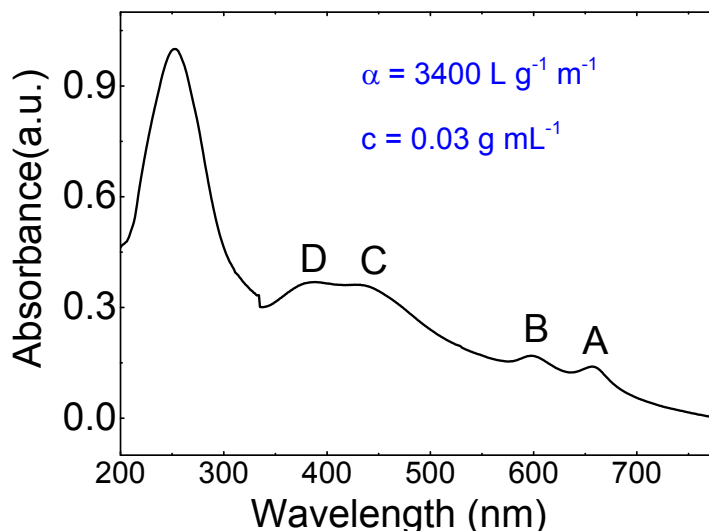
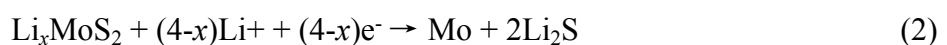


Figure S2. Absorption spectra of exfoliated MoS₂

S3. Cyclic voltammogram MoS₂ and MoS₂/C electrodes

The cyclic voltammetry measurement is carried out with the scan rate of 0.5 mVs⁻¹ over the potential range from 3.00 to 0.005 V vs Li/Li⁺. Figure S3 shows the 1st, 2nd and 3rd CV curves of MoS₂ electrode. In the 1st cycle, the first reduction peaks at ~1.03 V links to the formation of Li_xMoS₂ by the intercalation of Li⁺ into MoS₂ layers. The small reduction peak at ~0.70 V is attributed to the decomposition of electrolyte, resulting in the formation of solid electrolyte interface (SEI) on surface MoS₂ electrode.⁹ The reduction peak at ~0.46 V associated with the formation of Li₂S and metallic Mo nanoparticles via a conversion reaction of Li_xMoS₂.⁹⁻¹¹ The pronounced oxidation peak at ~2.32 V, is attributed to oxidation of Li₂S into Li⁺ and sulphur.⁹⁻¹¹ Meanwhile, the broad and weak oxidation peak at ~1.63 V, indicates the partial oxidation of metallic Mo to form MoS₂.^{12, 13} In the 2nd cycle, a new reduction peak at ~1.90 V is observed, which corresponds to the reduction of sulphur to form Li₂S. Besides, the oxidation peak is observed at ~2.32 V, attributed to oxidation of Li₂S. The two reduction and oxidation peaks in 2nd cycle constitute a reversible redox couple.⁹⁻¹¹ From the 2nd cycle, the electrochemical mechanism of MoS₂ is mainly dominated by the reversible conversion reaction of sulphur to Li₂S.¹⁴ In general, the two redox processes can be summarized according to the following reactions:⁹





However, the intensities of two reduction peaks (at ~ 1.03 and ~ 0.45 V) drastically decrease in the 2nd and 3rd cycles because of the consumption of residual MoS_2 , which is not completely reduced during the 1st cycle. From 3rd cycle, the intensity of reduction peak at ~ 1.90 V is slightly increased (24.9 mA g^{-1}) with respect to the 2nd cycle, which is attributed to an activation process of the electrode materials.¹⁵ Importantly, in the case of MoS_2 and $\text{MoS}_2/\text{C-1}$ electrodes, it is observed that the intensities of oxidation peaks at ~ 2.32 V significantly decrease with the increasing of cycle number. In specific, the intensity differences of these peaks between 1st and 2nd cycles are 45 mA g^{-1} and 18 mA g^{-1} for MoS_2 and $\text{MoS}_2/\text{C-1}$ electrodes, respectively. These CV behaviours suggest that the in the case of MoS_2 electrode, irreversible electrochemical processes take place due to irreversible redox reactions during lithiation/de-lithiation (equations 3 and 4).¹² These irreversible redox reactions progressively produce insulated sulfur (S) (see Figure S6) which can hinder the electron transport of MoS_2 electrode during cycling, resulting in its irreversible electrochemical processes¹⁶. These irreversible electrochemical processes are alleviated in the case of $\text{MoS}_2/\text{C-1}$ electrode due to the support of carbon network. However, the irreversible electrochemical processes are still taking place because the insufficient carbon content cannot completely cover all MoS_2 flakes in the case of $\text{MoS}_2/\text{C-1}$ electrode (see HR-TEM images, Figure 2d), which still can not completely improves the electron transport within the electrode.

For $\text{MoS}_2/\text{C-2}$ and $\text{MoS}_2/\text{C-3}$ electrodes (Figure S3c and d), the intensities of oxidation peaks at ~ 2.32 V in the initial three cycles are overlapped. The $\text{MoS}_2/\text{C-2}$ and $\text{MoS}_2/\text{C-3}$ electrodes exhibit a reversible electrochemical process, in contrast to MoS_2 and $\text{MoS}_2/\text{C-1}$ electrodes which do not present this process, indicating that the sufficient carbon content improves the electrical conductivity of MoS_2 . It is noteworthy to mention that the potential differences between redox peaks at ~ 1.92 and 2.32 V, after 3 cycles, is 440, 390, 330 and 350 mV, for MoS_2 , $\text{MoS}_2/\text{C-1}$, $\text{MoS}_2/\text{C-2}$ and $\text{MoS}_2/\text{C-3}$ electrodes, respectively. This fact confirms that MoS_2/C electrodes have lower overall resistance and better electrochemical reversibility than in the MoS_2 electrode.^{17, 18} As the carbon content increase, a widening of the cathodic peak set at ~ 0.46 V Li^+/Li , together with a slight reduction of the peak current, is observed. This modification finds its explanation in kinetics limitation, *i.e.* lithium diffusion through carbon thickness, of $\text{Li}_x\text{MoS}_2 - \text{Li}_2\text{S}$ conversion buffered by carbon network.

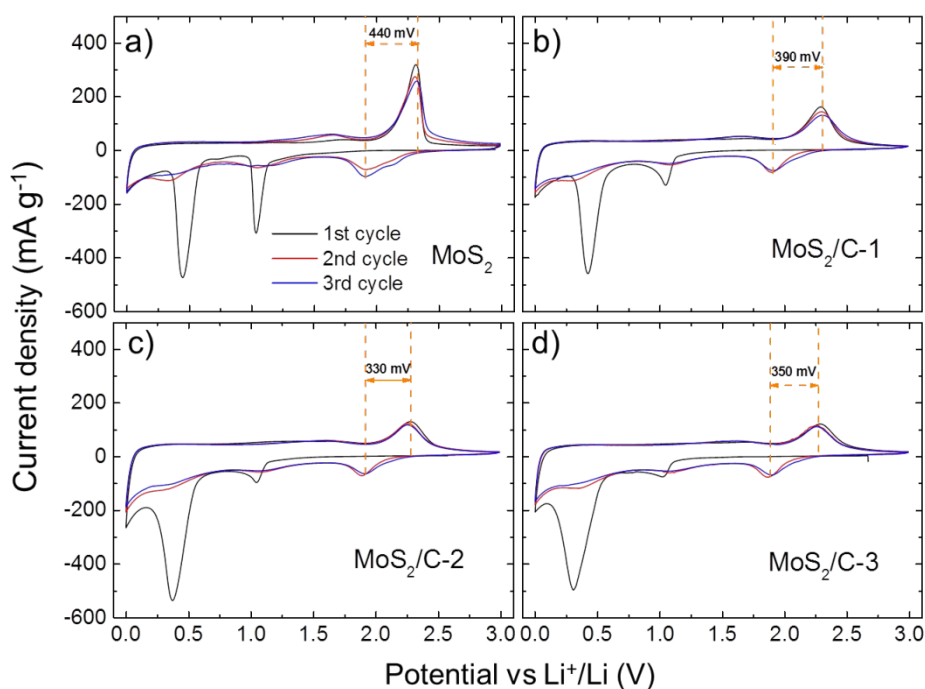


Figure S3. Cyclic voltammograms of (a) MoS_2 , (b) $\text{MoS}_2/\text{C-1}$, (c) $\text{MoS}_2/\text{C-2}$ and (d) $\text{MoS}_2/\text{C-3}$ electrodes at a scan rate of $50 \mu\text{Vs}^{-1}$.

S4. Electrochemical properties of amorphous carbon

The amorphous carbon is produced by the thermal decomposition of only PAA; the annealing profile of amorphous carbon is same as that of MoS_2/C composites see Experimental in the main text. The electrode slurries are prepared by dispersing amorphous carbon powder (active material), carbon black, and PAA with a weight ratio of 8:1:1 in IPA. The slurry is pasted onto copper disks with diameter of 1.5 cm. The disk is then dried in an oven (BÜCHI, B-585) at 60°C and 10^{-3} bar pressure for 12 hours. The amorphous carbon electrode is tested in half-cell configurations against Li foils (Sigma-Aldrich) as the counter and reference electrodes (two electrodes system). The assembling of half-cell follows the same procedure as MoS_2 and MoS_2/C based half-cells, see Experimental in the main text.

Galvanostatic charge/discharge cycling measurements are conducted at a current density of 100 mA g^{-1} over the potential range from 3.00 to 0.005 V vs Li/Li^+ in order to fully investigate electrochemical response for the Li^+ storage of the amorphous carbon electrodes. As shown in Figure S4, the voltage profile of amorphous carbon electrode shows the specific capacity of $\sim 285 \text{ mAh g}^{-1}$ in the initial charge process (lithiation). From subsequent charge processes, the electrode exhibits the continuously capacity fading of ~ 145 , 117 and 94 mAh g^{-1} corresponding to the 2nd, 5th and 20th cycles, respectively. The capacity fading during cycling suggests the irreversible Li^+ storage process of amorphous carbon electrode. This can be attributed to the presence of active sites, *e.g.*, defects in amorphous carbon.¹⁹⁻²¹ The irreversible Li^+ storage in amorphous carbon also contributes to the irreversible capacities of MoS_2/C electrode (see Figure 4 in the main text)

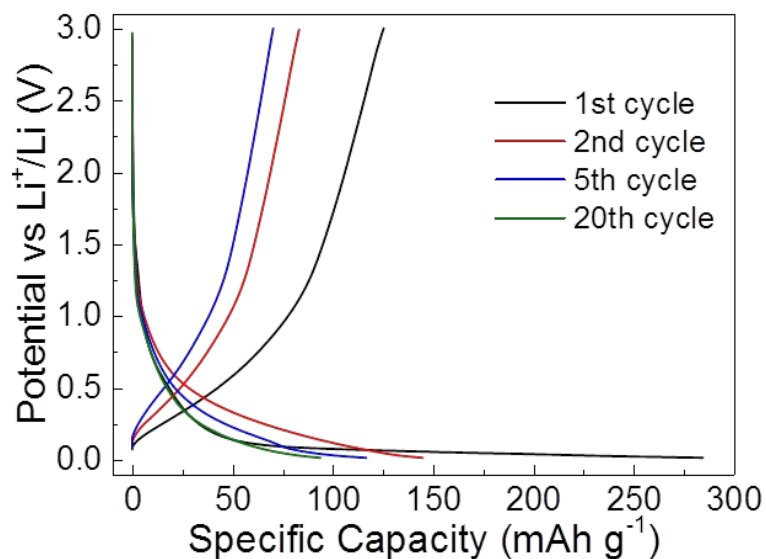


Figure S4. Voltage profiles upon galvanostatic charge/discharge of amorphous carbon

S5. Electrochemical properties of bulk MoS₂ and carbon-coated bulk MoS₂ (bulk MoS₂/C) electrodes

The preparation of bulk MoS₂/C powder with the weight ratio of bulk MoS₂:PAA=1:1, is same as the preparation of MoS₂/C composites, which has been reported in experimental session (see the main text). The electrode slurries are prepared by homogeneously dispersing bulk MoS₂ bulk MoS₂/C powders (active material), carbon black, and PAA with a weight ratio of 8:1:1 in IPA. The slurries are spread onto copper disks with diameter of 1.5 cm and then dried in an oven at 60° C and 10⁻³ bar pressure for 12 hours in oven (BÜCHI, B-585) to remove residual IPA. The mass loading of active materials (~1.0 mg) for each anode is calculated by subtracting the weight of bare Cu disks (using an analytical balance of Mettler Toledo XSE104) from the total weight of the electrode. The cycling performance of bulk MoS₂, bulk MoS₂/C electrodes at a current density of 100 mA g⁻¹ are shown in Figure S3, together with their Coulombic efficiencies. The bulk MoS₂ electrode delivers fast capacity fading after 100 cycles. This is mainly due to the volume change of bulk MoS₂ (black plots) during lithiation/de-lithiation, leading the pulverization of electrode.²²⁻²⁴ The capacity fading still appeared in the case of bulk MoS₂/C electrode (orange plots), however, it is less serious than that of bulk MoS₂ electrode. It suggests the role of carbon as buffer layer to limit the volume change of bulk MoS₂. However, the micro-size of bulk MoS₂ coupling with the insufficient of carbon content is a reason of capacity fading in bulk MoS₂/C electrode.

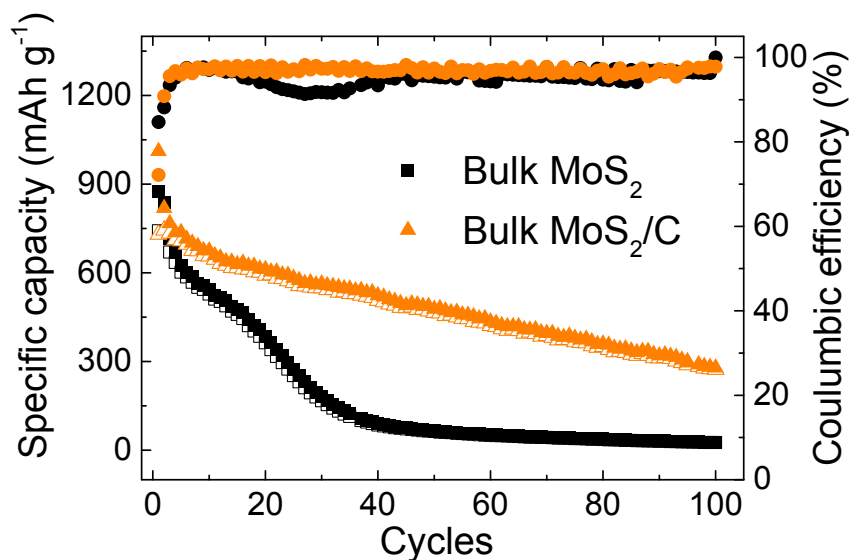
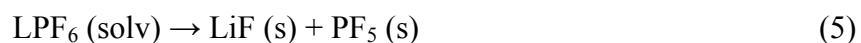


Figure S5. Specific capacity and Coulombic efficiency over charge/discharge galvanostatic cycles at 100 mA g⁻¹ of bulk MoS₂ and bulk MoS₂/C electrodes

S6. Elemental maps using scanning TEM (STEM)-energetic dispersive spectroscopy (EDS) of pristine MoS₂ electrode after cycling

Elemental mapping of materials from pristine MoS₂ electrode after 100 charge/discharge cycles is carried out by STEM-EDS measurements. Figure S6a shows a high angular annular dark field (HAADF)-STEM image of MoS₂ electrode materials, for which the corresponding elemental maps are demonstrated in Figure S6b-f. Carbon originates from the binder (PAA) and conductive agent (carbon black super-P). S is distributed in the particles labelled by the yellow dashed lines, while no Mo is detected in these particles. The presence of S alone confirms these particles are not MoS₂, but insulating S or Li₂S which can hinder the electron transport, leading to irreversible electrochemical processes of MoS₂ electrode (see Figure S3a).^{9, 15, 16}

The distribution of fluorine (F) and phosphorus (P) on the electrode can be used to identify the formation of SEI. The components of SEI are always contributed from the reduction and decomposition of the electrolyte. In this work, the LiPF₆ is used as the Li salt (see the Experimental in main text), which decomposes into LiF (s) and a small portion of PF₅ (s) through the reactions (5) (see the equation below).^{25, 26} The presence of F confirms the formation of LiF, while P is barely visible probably due to small amount of PF₅ in the observed area.



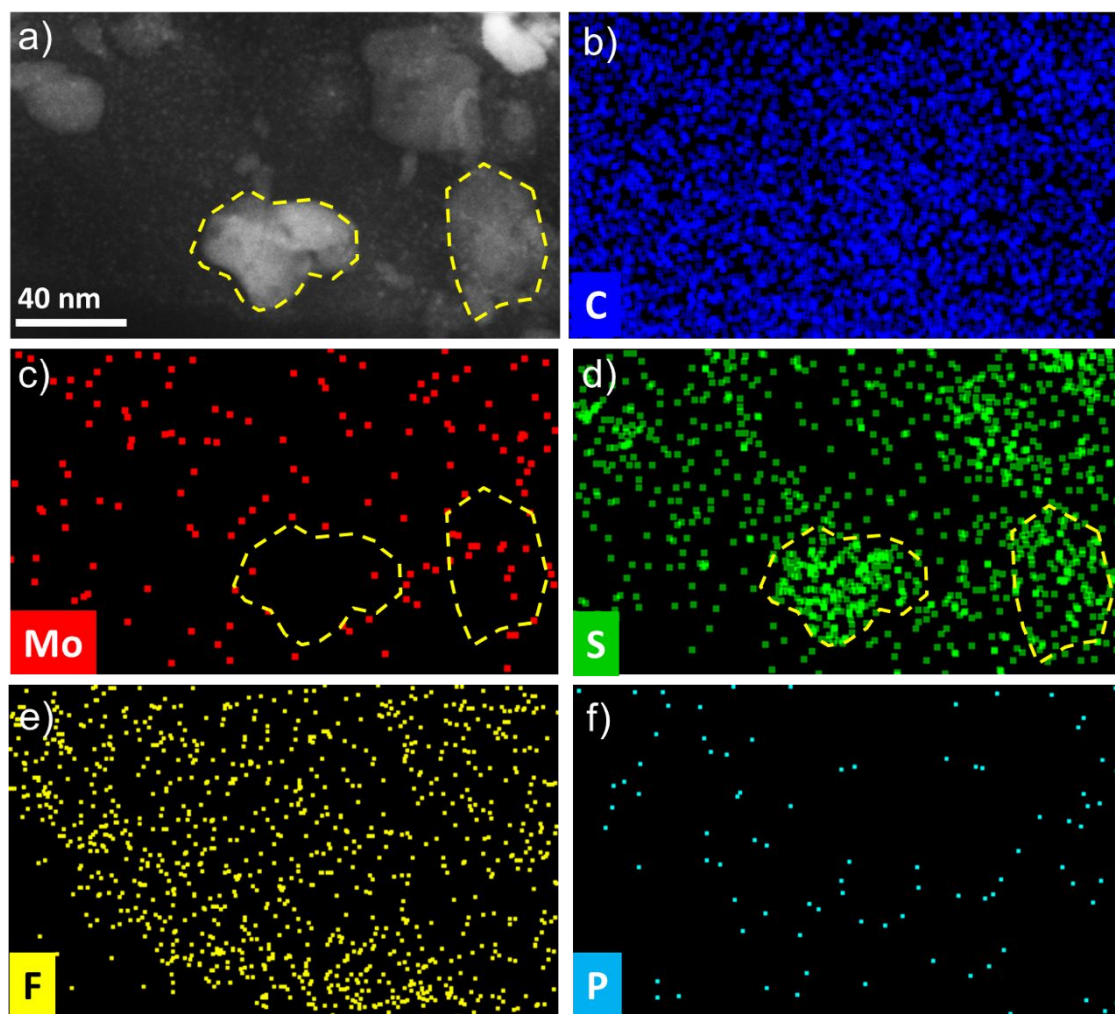


Figure S6. (a) HAADF-STEM image of MoS₂ electrode after 100 charge/discharge galvanostatic cycles and elemental maps of (b) C, (c) Mo, (d) S, (e) F and (f) P acquired by STEM-EDS.

S7. Fitting of electrochemical impedance spectra of MoS₂ and MoS₂/C electrodes after first cycle, at charged state.

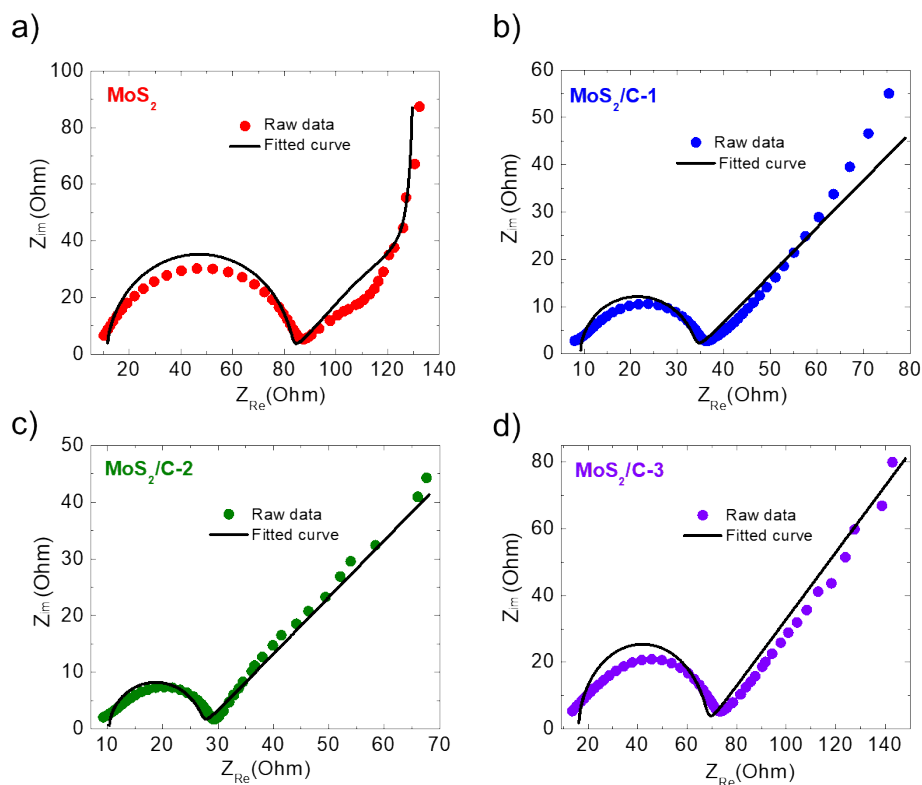


Figure S7. Fitting of Nyquist plots of MoS₂ (a), MoS₂/C-1 (b), MoS₂/C-2 (c), MoS₂/C-3 (d) electrodes after first cycle, at charged state.

S8. Fitting of electrochemical impedance spectra of MoS₂ and MoS₂/C samples after 100th cycle, at charged state

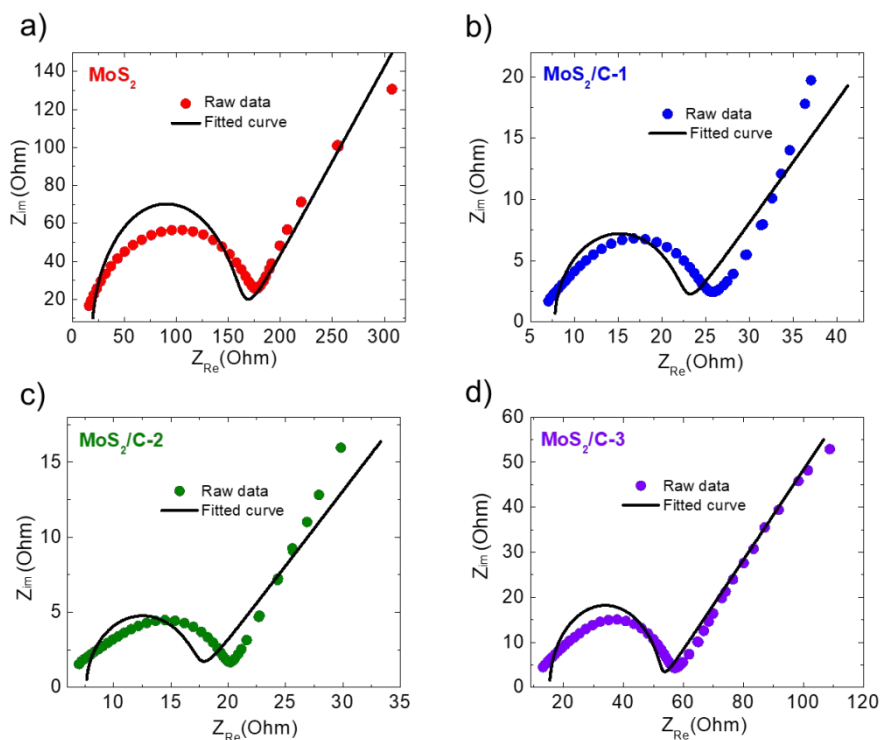


Figure S8. Fitting of Nyquist plots of MoS₂ (a), MoS₂/C-1 (b), MoS₂/C-2 (c), MoS₂/C-3 (d) electrodes after 100th cycle, at charged state.

The nyquist plots of MoS₂ and MoS₂/C electrodes after 1st cycle and after 100th cycle, at charged state are fitted via EC-Lab software, powered by Bio-Logic Inc. According to the fitting results, the nyquist plots of all electrodes consist of a depressed semi-circle in the high frequency region and a sloping straight line in the low-frequency region. The semi-circles are described by means of a generalized RC-circuit (the inset in Figure 4a) with electrolyte resistance R_E (resistance caused by the mass transport of Li⁺ through electrolyte), charge transfer resistance (R_{CT}) (including the electron transfer to the reactive centre (MoS₂), and a constant phase element (CPE) for the electrode/electrolyte interface. The high frequency region is associated with the R_{CT} , whereas the low-frequency line is descriptive of the Li⁺ diffusion impedance within electrode which is described by the Warburg circuit element (Z_W) in RC-circuit.

S9. Thermogravimetric analysis of MoS₂ and MoS₂/C composites

As shown in Figure 2a in the main text, the derivative weight curve of MoS₂ sample (red dash-curve) shows the first weight loss mainly occurs from ~ 350°C to 470°C, which is attributed to oxidation of MoS₂ to MoO₃,¹¹ and the weight loss of sulfur is calculated ~ 11.2 wt%. As presented in table 1, the weight loss of sulfur and carbon is estimated approximately ~ 21.3, 27.3 and 41.1 wt% for MoS₂/C-1, MoS₂/C-2, MoS₂/C-3 sample, respectively. The weight of carbon in each MoS₂/C samples are calculated by the subtracting the weight losses of sulfur and carbon (wt%) to weight loss of sulfur (11.2 wt%). As a result, the carbon contents in MoS₂/C-1, MoS₂/C-2, and MoS₂/C-3 samples are estimated to be ~ 10.1, 16.1 and 29.9 wt%.

Table S1. Calculation of wt% of carbon based on TGA measurement.

Samples	Wt% of MoS ₂ : PAA	Weight loss of Sulfur and Carbon (%)	Weight of carbon (%)
MoS ₂ /C-1	1 : 1	21.22	10.00
MoS ₂ /C-2	1 : 2	27.33	16.11
MoS ₂ /C-3	1 : 4	41.08	29.86

References

- (1) Yu, Y. F.; Li, C.; Liu, Y.; Su, L. Q.; Zhang, Y.; Cao, L. Y. Controlled Scalable Synthesis of Uniform, High-Quality Monolayer and Few-layer MoS₂ Films. *Sci Rep-Uk* **2013**, 3.

- (2) McCreary, K. M.; Hanbicki, A. T.; Robinson, J. T.; Cobas, E.; Culbertson, J. C.; Friedman, A. L.; Jernigan, G. G.; Jonker, B. T. Large-Area Synthesis of Continuous and Uniform MoS₂ Monolayer Films on Graphene. *Adv Funct Mater* **2014**, 24, 6449-6454.
- (3) Lee, C.; Yan, H.; Brus, L. E.; Heinz, T. F.; Hone, J.; Ryu, S. Anomalous Lattice Vibrations of Single- and Few-Layer MoS₂. *Acs Nano* **2010**, 4, 2695-2700.
- (4) Qiu, D. Y.; da Jornada, F. H.; Louie, S. G. Optical Spectrum of MoS₂: Many-Body Effects and Diversity of Exciton States. *Phys Rev Lett* **2013**, 111.
- (5) Xu, S. J.; Li, D.; Wu, P. Y. One-Pot, Facile, and Versatile Synthesis of Monolayer MoS₂/WS₂ Quantum Dots as Bioimaging Probes and Efficient Electrocatalysts for Hydrogen Evolution Reaction. *Adv Funct Mater* **2015**, 25, 1127-1136.
- (6) Nguyen, E. P.; Carey, B. J.; Daeneke, T.; Ou, J. Z.; Latham, K.; Zhuiykov, S.; Kalantar-zadeh, K. Investigation of Two-Solvent Grinding-Assisted Liquid Phase Exfoliation of Layered MoS₂. *Chem Mater* **2015**, 27, 53-59.
- (7) Kozawa, D.; Kumar, R.; Carvalho, A.; Amara, K. K.; Zhao, W. J.; Wang, S. F.; Toh, M. L.; Ribeiro, R. M.; Neto, A. H. C.; Matsuda, K. et al. Photocarrier relaxation pathway in two-dimensional semiconducting transition metal dichalcogenides. *Nat Commun* **2014**, 5.
- (8) Coleman, J. N.; Lotya, M.; O'Neill, A.; Bergin, S. D.; King, P. J.; Khan, U.; Young, K.; Gaucher, A.; De, S.; Smith, R. J. et al. Two-Dimensional Nanosheets Produced by Liquid Exfoliation of Layered Materials. *Science* **2011**, 331, 568-571.
- (9) Stephenson, T.; Li, Z.; Olsen, B.; Mitlin, D. Lithium ion battery applications of molybdenum disulfide (MoS₂) nanocomposites. *Energ Environ Sci* **2014**, 7, 209-231.
- (10) Fang, X. P.; Hua, C. X.; Guo, X. W.; Hu, Y. S.; Wang, Z. X.; Gao, X. P.; Wu, F.; Wang, J. Z.; Chen, L. Q. Lithium storage in commercial MoS₂ in different potential ranges. *Electrochim Acta* **2012**, 81, 155-160.

- (11) Zhang, Y. F.; Wang, Y.; Yang, J.; Shi, W. H.; Yang, H. Y.; Huang, W.; Dong, X. C. MoS₂ coated hollow carbon spheres for anodes of lithium ion batteries. *2d Mater* **2016**, 3.
- (12) Hu, S.; Chen, W.; Zhou, J.; Yin, F.; Uchaker, E.; Zhang, Q. F.; Cao, G. Z. Preparation of carbon coated MoS₂ flower-like nanostructure with self-assembled nanosheets as high-performance lithium-ion battery anodes. *J Mater Chem A* **2014**, 2, 7862-7872.
- (13) Jiang, H.; Ren, D. Y.; Wang, H. F.; Hu, Y. J.; Guo, S. J.; Yuan, H. Y.; Hu, P. J.; Zhang, L.; Li, C. Z. 2D Monolayer MoS₂-Carbon Interoverlapped Superstructure: Engineering Ideal Atomic Interface for Lithium Ion Storage. *Adv Mater* **2015**, 27, 3687-3695.
- (14) Xiao, J.; Wang, X. J.; Yang, X. Q.; Xun, S. D.; Liu, G.; Koech, P. K.; Liu, J.; Lemmon, J. P. Electrochemically Induced High Capacity Displacement Reaction of PEO/MoS₂/Graphene Nanocomposites with Lithium. *Adv Funct Mater* **2011**, 21, 2840-2846.
- (15) Xue, Q. F.; Chen, G. T.; Liu, M. Y.; Xiao, J. Y.; Chen, Z. M.; Hu, Z. C.; Jiang, X. F.; Zhang, B.; Huang, F.; Yang, W. et al. Improving Film Formation and Photovoltage of Highly Efficient Inverted-Type Perovskite Solar Cells through the Incorporation of New Polymeric Hole Selective Layers. *Adv Energy Mater* **2016**, 6.
- (16) Borchardt, L.; Oschatz, M.; Kaskel, S. Carbon Materials for Lithium Sulfur Batteries-Ten Critical Questions. *Chem-Eur J* **2016**, 22, 7324-7351.
- (17) Shen, L. F.; Uchaker, E.; Zhang, X. G.; Cao, G. Z. Hydrogenated Li₄Ti₅O₁₂ Nanowire Arrays for High Rate Lithium Ion Batteries. *Adv Mater* **2012**, 24, 6502-6506.
- (18) Hu, S.; Chen, W.; Uchaker, E.; Zhou, J.; Cao, G. Z. Mesoporous Carbon Nanofibers Embedded with MoS₂ Nanocrystals for Extraordinary Li-ion Storage. *Chem-Eur J* **2015**, 21, 18248-18257.
- (19) Mukai, S. R.; Hasegawa, T.; Takagi, M.; Tamon, H. Reduction of irreversible capacities of amorphous carbon materials for lithium ion battery anodes by Li₂CO₃ addition. *Carbon* **2004**, 42, 837-842.

- (20) Qiu, W. D.; Xia, J.; He, S. X.; Xu, H. J.; Zhong, H. M.; Chen, L. P. Facile Synthesis of Hollow MoS₂ Microspheres/Amorphous Carbon Composites and Their Lithium Storage Properties. *Electrochim Acta* **2014**, 117, 145-152.
- (21) Chang, K.; Chen, W. X.; Ma, L.; Li, H.; Li, H.; Huang, F. H.; Xu, Z. D.; Zhang, Q. B.; Lee, J. Y. Graphene-like MoS₂/amorphous carbon composites with high capacity and excellent stability as anode materials for lithium ion batteries. *J Mater Chem* **2011**, 21, 6251-6257.
- (22) Wan, Z. M.; Shao, J.; Yun, J. J.; Zheng, H. Y.; Gao, T.; Shen, M.; Qu, Q. T.; Zheng, H. H. Core-Shell Structure of Hierarchical Quasi-Hollow MoS₂ Microspheres Encapsulated Porous Carbon as Stable Anode for Li-Ion Batteries. *Small* **2014**, 10, 4975-4981.
- (23) Wang, H. Y.; Ren, D. Y.; Zhu, Z. J.; Saha, P.; Jiang, H.; Li, C. Z. Few-layer MoS₂ nanosheets incorporated into hierarchical porous carbon for lithium-ion batteries. *Chem Eng J* **2016**, 288, 179-184.
- (24) Lee, G. H.; Kim, S. J.; Kim, M. C.; Choe, H. S.; Kim, D. M.; Han, S. B.; Kwak, D. H.; Jeong, J. H.; Park, K. W. In situ formation of MoS₂/C nanocomposite as an anode for high-performance lithium-ion batteries. *Rsc Adv* **2016**, 6, 92259-92266.
- (25) Andersson, A. M.; Edstrom, K. Chemical composition and morphology of the elevated temperature SEI on graphite. *J Electrochem Soc* **2001**, 148, A1100-A1109.
- (26) Edstrom, K.; Andersson, A. M.; Bishop, A.; Fransson, L.; Lindgren, J.; Hussenius, A. Carbon electrode morphology and thermal stability of the passivation layer. *J Power Sources* **2001**, 97-98, 87-91.